

Article

Accuracy of Mean Radiant Temperature Derived from Active and Passive Radiometry

Henning Staiger ^{1,*} and Andreas Matzarakis ² ¹ Emeritus Deutscher Wetterdienst, Corneliusstr. 2a, 64546 Mörfelden-Walldorf, Germany² Research Centre Human Biometeorology, Deutscher Wetterdienst, Stefan-Meier-Str. 4, 79104 Freiburg, Germany; andreas.matzarakis@dwd.de

* Correspondence: henning.staiger@gmx.de; Tel.: +49-6105-4043-782

Received: 9 June 2020; Accepted: 27 July 2020; Published: 30 July 2020



Abstract: The concept of the mean radiant temperature (T_{mrt}) allows the study of radiative exchanges between a human and its environment. It presupposes that the radiant effects on the person of the actual environment, which is generally heterogeneous, and the virtual environment, which is defined as homogeneous, are identical. ISO 7726 specifies the required accuracy in T_{mrt} as input of rational thermal indices, outdoors ± 5 (K). T_{mrt} accounts for the radiant heat absorbed by skin/clothing from the shortwave (SW) and longwave (LW) spectral bands. Most of the radiant components are isotropic. However, there are anisotropic SW components; namely the direct irradiance and under clear or partly obstructed skies a significant circumsolar fraction (f_{cs}) in the diffuse irradiance. Both originate from the close proximity of the solar disk. This study highlights the effect of f_{cs} on T_{mrt} . In the scope of human biometeorology a standing body posture is standard. For unidirectional irradiances its radiant cross-section varies dependent on the solar altitude. Active radiometry in deriving T_{mrt} is based on measured irradiances. One method is the Klima-Michel-Modell (KMM) that uses readily available measurements from standard meteorologically radiant observations. KMM references Fanger's area projection factors that are derived from precise measurements of real humans. Thus, KMM serves as reference in evaluation of further methods. One is the six-directional instrument ($T_{\text{mrt},r,6\text{-Dir}}$). Slightly simplifying a standing human, it represents a subject as a rectangular solid. $T_{\text{mrt},r,6\text{-Dir}}$ is derived based on measured irradiances incident on the vertical and horizontal planes. In passive radiometry the energy balance equation of a black globe thermometer is solved that leads to $T_{\text{mrt},Tg,BG}$. f_{cs} significantly impacts T_{mrt} with noticeably reduced values for high and increased for low solar altitudes. Hence, accounting for f_{cs} is essential for the accuracy of T_{mrt} . For KMM an extension to an existing algorithm is provided in order to include f_{cs} into the T_{mrt} calculation that results in $T_{\text{mrt},r,KMM}$. For $T_{\text{mrt},r,6\text{-Dir}}$ the radiant cross-section of the solid depends to a minor extent on its azimuth relative to the solar azimuth. As a result $T_{\text{mrt},r,6\text{-Dir}}$ slightly scatters compared to $T_{\text{mrt},r,KMM}$. However, it remains within ± 2 (K). $T_{\text{mrt},Tg,BG}$ compared to $T_{\text{mrt},r,KMM}$ complies only at night with the ISO 7726 bin of ± 5 K. $T_{\text{mrt},Tg,BG}$ significantly overestimates $T_{\text{mrt},r,KMM}$ during the daytime, because of its greater SW absorptance compared to skin/clothing and to a smaller extent because the standing posture is represented by a sphere. Particularly in sunny conditions, $T_{\text{mrt},Tg,BG}$ is subject to considerable variance. Thus, outdoors during the daytime, $T_{\text{mrt},Tg,BG}$ is unable to serve as an appropriate input for the calculation of rational-based thermal indices.

Keywords: mean radiant temperature; black globe temperature; solar short- and terrestrial long-wave down- and upward radiant flux densities; direct and diffuse solar irradiance components; anisotropic circumsolar fraction in diffuse irradiance

1. Introduction

Human biometeorology is the interdisciplinary field of science that studies interactions between the human body and the Earth's atmosphere and it is thus related to outdoor environments. Especially, it is concerned with contingency planning, health protection, regional and urban planning, the design of open spaces, various aspects of tourism and recreation areas, as well as research in climate change [1]. Its results are used in heat warnings and to provide medical-related information for weather forecasting. All these facets require a rational, thermophysiological consistent assessment of the human thermal environment. This is frequently accomplished by applying thermal indices. Rational thermal indices are based on complete human energy budget models consisting of both a controlled passive and a controlling active system [2]. They require six basic parameters in order to define the human thermal environment. These are four meteorological variables, namely air temperature (t_a (°C) or T_a (K)), water vapor pressure (e_a (hPa)), air velocity (v_a (m/s)) and mean radiant temperature (T_{mrt} (K) or t_{mrt} (°C)), plus two inputs that describe properties affecting the human body: the insulation of clothing worn and the activity of the person described in terms of net metabolic heat production [3].

Compared to t_a , e_a and v_a , which can readily and accurately be measured, T_{mrt} is the most complex of the four meteorological inputs [1,4]: it is the uniform temperature of an imaginary black enclosure (emissivity $\varepsilon = 1$), in which a human body of defined azimuth and posture would gain the same radiant heat as in the actual nonuniform enclosure [5–8]. T_{mrt} assesses the impact of the solar shortwave (SW, 0.3–3 μm) and the terrestrial (thermal) longwave (LW, 3–50 μm) radiant components on the human energy balance.

The concept of T_{mrt} allows the study of radiative exchanges between a human person and its environment. Because it presupposes that the radiant effects on the person of the actual environment which is generally heterogeneous and the virtual environment which is defined as homogeneous are identical, it facilitates thermophysiological modeling [5,8]. T_{mrt} is a direct measure of the environmental sensible heat stress onto the body that come from radiation. The rational indices resulting from thermophysiological modeling and their application require sufficient accuracy of T_{mrt} . Those are quantified by ISO 7726 according to the extent of the thermal annoyance to be assessed.

The calculation of T_{mrt} is originally developed for indoor applications. In a room, T_{mrt} may be calculated from the surface temperatures T_N of the surrounding N surfaces with uniform temperature each by accounting for the angle factor F_{p-N} between a person and the surrounding surfaces [6,8,9]:

$$T_{\text{mrt}}^4 = T_1^4 \cdot F_{p-1} + T_2^4 \cdot F_{p-2} + \dots + T_N^4 \cdot F_{p-N} \quad (1)$$

F_{p-N} is a function of the shape, the size and the relative position of surface N in relation to the person. The position of the surface N is described in spherical coordinates by azimuth and elevation angles. The angle factor can precisely but elaborately be determined by numerical integration over the azimuth and elevation angles. The integration takes place between the normal of the person's location on the concerned surface up to the angle of N . F_{p-N} consists of the projected area factor f_p that is weighted according to the relative position of surface N to the person. $f_p = A_p/A_{\text{eff}}$ relates the projected area of a person A_p to its effective radiant area A_{eff} , i.e., the total surface of the person minus that area parts that overlap, e.g., arms and trunk. Thus, f_p is a function of the body posture and the elevation angle [6,10,11] and is precisely determined by the shadow area of the irradiated person on a plane normal to the direction of the incident beam. As the sum of the angle factors is unity, the fourth power of T_{mrt} will be seen to be equal to the mean value of the surrounding surface temperatures to the fourth power, weighted with the respective angle factors [6].

By inversion of the Stefan–Boltzmann law, the T_N^4 in Equation (1) can be replaced by measured irradiances, i.e., by active radiometry. Thus, measured radiant flux densities of the effective components in the SW and LW spectral bands can directly be applied. This is the base for outdoor use within the scope of human biometeorology where surface temperatures of the upper (atmospheric) half space are in principle not available.

In applied human biometeorology an upright reference subject is used that is rotationally symmetric to its vertical axis because the azimuthal orientation of the subject is usually unknown. Its elevation dependent f_p is derivable from diagrams and tables [1,6,11]. Because only the fraction of radiant energy that is absorbed by the skin/clothing surface can have an effect on the human energy balance, the clothing/skin of the reference subject is assumed to show overall SW absorption ($\alpha_{sw,sk}$) of 0.70 and LW emissivity ($\epsilon_{lw,sk}$) of 0.97 that is identical with its absorptivity (Kirchhoff law) [1,8,9].

In the scope of human biometeorology, two methods that apply active radiometry are in use. One [12] bases on operationally available radiant flux densities as they, for example, are recorded by meteorological services according to guidelines of the World Meteorological Organization [13,14]. The other applies the definition of plane radiant temperature [8,9]. It uses measured SW and LW radiant flux densities onto the six planes of a rectangular solid that represents a human of standing body posture [1,15].

Another approach to determine T_{mrt} is passive radiometry. Here, T_{mrt} is indirectly derived by determining the energy balance of a measuring system, especially the black globe thermometer [8,16,17]. The method has a long history and provides in those early years at least estimates of T_{mrt} where the measurement of radiant flux densities was complex due to technical reasons and expensive [16,17]. The black globe was originally introduced in order to measure radiant heat indoors in relation to human comfort [17]. However, it is also applied outdoors, where it is integrated in instruments that provide the measured base for the calculation of the wet-bulb-globe-temperature index [18,19]. In the scope of human bioclimatology, the black globe is now also being used outdoors in the form of a matt black-painted table-tennis ball [20,21]. T_{mrt} derived from the black globe is an approximation due to the difference in shape between a person and a globe [8]. In particular, direct SW irradiation at high solar altitudes will be over-estimated by the globe in relation to that received by a standing person. The black globe differs strongly in the SW absorptance compared to the outer surface of a clothed person. Furthermore, the accuracy of measuring T_{mrt} using a black globe can vary to a great extent according to the values for the other characteristics of the environment [8,22].

The occurrence of heat stress situations is usually related to clear sky conditions, when humans are directly exposed to intense, frequently asymmetric irradiation. In this case, the diffuse radiant intensity from the sun's direction is substantially higher than from the remaining upper half space [23–25] and may significantly affect T_{mrt} especially for the standing body posture.

This study aims to assess the three methods for outdoor use. In particular, it shall be evaluated whether the achieved accuracy is sufficient that the derived T_{mrt} can serve as input for the calculation of thermal indices. Furthermore, it shall be investigated how the circumsolar anisotropy in the diffuse radiant component affects T_{mrt} .

The objectives are accomplished by defining the effective solar and terrestrial irradiances in section "Methods and Materials", in which the methods and their theoretical background are shortly described and the available data for their evaluation are presented. The assessment methodology including the method selected for reference is introduced. Based on these data, the accuracy of the remaining methods is evaluated against the reference in section "Results" and the issue is examined how the circumsolar anisotropy in the diffuse SW irradiance affects T_{mrt} .

2. Methods and Materials

2.1. Effective Solar and Terrestrial Irradiances

Solar electromagnetic irradiation that reaches the earth's surface covers a spectral range between ~280 and 3000 nm. There are different impacts on the human organism depending upon the spectrum. The wavelengths between 400 and 730 nm enable photopic and scotopic vision. Especially in the UV-B range ≤ 315 nm, the impact on the skin may be harmful. Dependent on the dose and the skin type, it can provoke an erythema. However, the predominant impact of SW and LW irradiance on the skin is thermal. It is spectrally independent as long as the intensities in a given spectral range are less than

1000 (W/m²). Thus, it is the total intensity or energy that affects a person's thermal psycho-physiological state [26]. Hence, it is to be concluded that T_{mrt} can be derived for the relevant wavelength bands from spectrally integrating instruments. They are deployed as standard in meteorology.

The effective SW radiant flux densities (W/m²), are

- The downward direct irradiance (E_I) incident on a plane normal to the radiation's direction and measured by a pyrliometer. E_I is that part of the solar radiation that is not scattered by atmospheric constituents in its transfer to the earth's surface. Thus, E_I is unidirectional because it originates from the solar disk, i.e., it is anisotropic.
- The downward diffuse (directionally indistinguishable) irradiance (E_D) incident on a horizontal plane facing the upper half space and measured by a pyranometer combined with e.g., a shadow disk moved by a sun tracker or a shadow band. The latter requires subsequent correction of the reading, which accounts in particular for sky radiance anisotropy [23,27,28]. E_D is that part of the solar radiation that has been subjected to scattering by atmospheric atoms and molecules (Rayleigh) and by aerosol particles and cloud droplets (Mie). Scattering changes the direction of the incident beam, yet leaves its energy and frequency unchanged. E_D is multidirectional; frequently it impacts with the same amount of energy from all directions of the sky dome, and is then termed isotropic.
- The surface reflected irradiance (E_R) above the lower half space and incident on a horizontal plane facing downward and measured by a pyranometer. E_R is predominantly Lambertian equivalent reflected, i.e., it is diffuse. The direct mirror-like reflected proportion of E_R remains small and can be regarded as insignificant [29,30]. Thus, E_R is usually isotropic with regard to the lower half space. Exceptions to Lambertian reflection include water and ice surfaces.

However, the most frequently observed irradiance is the SW global irradiance (E_G) incident on a horizontal plane facing upward (pyranometer). E_G is defined as $E_G = E_I \cdot \sin(\gamma_s) + E_D$, where γ_s (degrees) is the solar elevation. Hence, measured E_G and E_D allow E_I to be determined, the measurement of which is more difficult. There are algorithms available that break measured E_G down into its fractions using a stochastic approach (see e.g., [31]).

E_R can also be attributed to E_G by $E_R = \rho_s \cdot E_G$. ρ_s is the surface albedo (0–1) that depends on ground surface properties. For a given location, ρ_s can frequently be regarded as constant, but there may be seasonal variations [32], e.g., due to snow cover in winter.

Under overcast skies, E_D is completely isotropic. However, under skies which are clear or only with low cloud cover, E_D includes a significant anisotropic fraction that is concentrated around the solar disk with a view angle of ≤ 12 (degree). This circumsolar brightening originates from Mie scattering caused by aerosols and cloud particles that has a narrow peak in the forward direction. This anisotropic circumsolar fraction (f_{cs}) of E_D is never available from operational observations. Hence, it must be derived using sky radiance models, e.g., that of Perez et al. [23], which accounts for γ_s , sky clearness (overcast to clear) and sky brightness (cloud thickness and/or aerosol loading ranging from low to high). f_{cs} is especially important if the irradiance on tilted surfaces is calculated (see e.g., [32]) because this depends on the azimuth of the radiation source, e.g., for an upright human.

The amount of radiation which each body emits depends on its (surface) temperature. Hence, the atmosphere and the ground are sources of electromagnetic radiation due to their temperature in the thermal-spectral range. The effective LW flux densities (W/m²), measured by pyrgeometers, are

- The isotropic diffuse downward thermal irradiance of the atmosphere (E_A) incident on a horizontal plane facing the upper half space;
- The upward isotropic diffuse irradiance of the lower half space (E_E) incident on a horizontal plane facing the lower half space. E_E includes the small fraction ($\leq 5\%$) of ground-reflected E_A .

2.2. Klima-Michel-Modell

The calculation of T_{mrt} inside the Klima-Michel-Modell (KMM) [12] is based on Equation (1) for outdoor use. Breaking the unidirectional irradiances originating from the area surrounding the solar disk down into a vertical and a horizontal component the respective angle factor F_{p-N} (Equation (1)) can be shown to equal $f_p(\gamma_s)$, because the weight in F_{p-N} that accounts for the relative position of surface N to the person is in this case unity. For the standing posture of a person rotationally symmetric to its vertical axis a parameterization for f_p based on diagrams in [6] can be applied (Figure 1) [12]:

$$f_p = 0.308 \times \cos \left\{ \gamma_s \times \left(0.998 - \frac{\gamma_s^2}{50000} \right) \right\}. \tag{2}$$

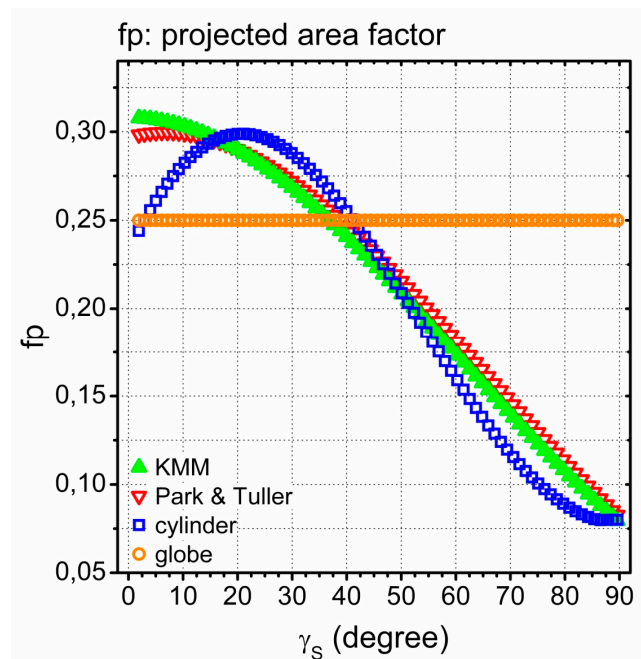


Figure 1. Projected area factor f_p : both Klima-Michel-Modell (KMM) [12] and Park and Tuller [11] for the reference subject and additionally for a cylinder and a globe.

For a surrounding free of significant horizon limitations [33], T_{mrt} can, therefore, be derived directly from measured radiant flux densities, active radiometry, referred to below by “r” in subscripts. Because the view angle of the circumsolar fraction of E_D is small, it can reasonably be treated like E_I as originating from the solar disk [24]. Then, the equation of Jendritzky et al. [12] for the calculation of T_{mrt} , which assumes $f_{cs} = 0$, can be extended for all f_{cs} . It reads:

$$T_{mrt,r,KMM} = \left\{ \frac{1}{\sigma_{SB}} \cdot \left[\begin{array}{l} f_a \cdot (E_A + E_E) \\ + \frac{\alpha_{sw,Sk}}{\epsilon_{lw,Sk}} \cdot \left(\begin{array}{l} f_a \cdot (E_R + (1 - f_{cs}) \cdot E_D) \\ + f_p \cdot \left(E_I + \frac{1}{\sin(\gamma_s)} \times f_{cs} \cdot E_D \right) \end{array} \right) \right] \right\}^{0.25} \tag{3}$$

$\sigma_{SB} = 5.67 \cdot 10^{-8} \text{ (W} \cdot \text{m}^{-2} \cdot \text{K}^{-4})$ is the Stefan–Boltzmann constant. Because isotropic diffuse radiation from one of two half spaces irradiates the body with the same intensity over all azimuth and elevation angles (Equation (1)), the integration over all angle factor F_{p-N} of this half space is $f_a = 0.5$, where f_a is independent of γ_s and the shape of the irradiated body [12,24,34]. Hereafter, the procedure based on Equation (3) is called $T_{mrt,r,KMM}$, relating it to the Klima-Michel-Modell (KMM) [12].

2.3. Six-Direction Instrument

Another method for determining T_{mrt} using observed irradiances is the six-directional instrument ($T_{mrt,r,6-Dir}$ (K)) that posits the subject concerned as a rectangular solid [1,15]. This $T_{mrt,r,6-Dir}$ (K) is also defined as the plane radiant temperature [8,9], however using pyranometers and pyrgeometers facing up-down, left-right, forwards-backwards and belongs so to active radiometry. The six instruments of each type may be replaced by one that can be rotated in the six directions to deliver a temporal sequence of observations. The six weighting factors (W_i) for the observed SW (K_i) and LW (L_i) radiant flux densities (W/m^2) are derived using Fanger’s formula [6] for f_p of a rotationally symmetric person who is standing. W_i equals 0.06 for up and down and 0.22 for the four cardinal points. The energy absorbed by the rectangular solid (S_r) is $\sum_{i=1}^6 W_i \cdot (\alpha_{sw,SK} \cdot K_i + \epsilon_{lw,SK} \cdot L_i)$ (W/m^2) and, thus

$$T_{mrt,r,6-Dir} = \left(\frac{S_r}{\sigma_{SB} \cdot \epsilon_{lw,SK}} \right)^{0.25} \tag{4}$$

2.4. Black Globe Thermometer

T_{mrt} can be derived indirectly by solving the energy balance equation of a measuring system that is affected by convection, conduction and radiation (passive radiometer). T_{mrt} is derivable when the system is in equilibrium, i.e., the radiant energy input is exactly balanced by convective heat dissipation [16]. The black globe thermometer is most frequently used for this [17]. This is essentially a hollow spherical globe containing an ordinary thermometer. The bulb of this thermometer is at the center of the sphere and theoretically represents the mean surface temperature of the sphere’s inner surface. This integral value is composed of individual values of SW and LW radiant flux densities of the actual environment that vary with the solid angle. However, they may be smoothed, dependent on the heat conductivity of the globe’s material.

The usual form of the black globe thermometer (BG) consists of a thin-walled (≈ 0.4 mm) copper sphere of diameter (d_g) of 0.15 (m) that is coated in matt black paint, emissivity $\epsilon_g = 0.95$ [8,22]. When exposed to radiation, such black globe thermometers usually register a higher temperature, the globe temperature (T_g (K) or t_g ($^{\circ}C$)), than an ordinary, radiation-protected thermometer that results in t_a . Generally, the transient heat balance of a globe at time t is [35,36]:

$$(Q_r(t) - Q_c(t))_{outer} - (Q_r(t) - Q_c(t))_{inner} = -A_g \cdot \delta_g \cdot \rho \cdot c \cdot \frac{dT_g}{dt} \tag{5}$$

$Q_r(t)$ and $Q_c(t)$ are the radiant and the convective heat transfer rates, respectively, evaluated for the outer and for the inner surface of the globe. The sphere’s surface (A_g) is $4 \cdot \pi \cdot d_g^2$ (m^2), and δ_g (m) is the shell’s thickness. ρ (kg/m^3) is the mass density of the shell’s material, and c ($J K^{-1} kg^{-1}$) its specific heat capacity. dt is a time interval. This balance equation neglects heat conduction across the surface. This is only justified for metallic (high thermal diffusivity) shells that are thin relative to their overall dimensions [35]. Over the whole globe, the heat loss from the inner surface is zero because elements of the inner globe radiate out to each other and internal, free convection air currents redistribute heat from one point to another [35,37]. However, the radiant properties of the inner surface and the mass of the thermometer’s bulb affect the time constant of the instrument. The energy balance on the globe’s outer surface yields [8,22,35,38,39]:

$$(Q_r(t) - Q_c(t))_{outer} = \sigma_{SB} \cdot \epsilon_g \cdot (T_{mrt}^4 - T_g^4) - \bar{h}_{c,g} \cdot (T_a - T_g) = -\delta_g \cdot \rho \cdot c \cdot \frac{dT_g}{dt} \tag{6}$$

$\bar{h}_{c,g}$ ($\text{W}\cdot\text{m}^{-2}\cdot\text{K}^{-1}$) is the convective heat transfer coefficient averaged over the surface of the sphere. In equilibrium, the right hand side of Equation (6) equals zero, $\lim_{t \rightarrow \infty} (Q_r(t) - Q_c(t))_{\text{outer}} = 0$, and, then, Equation (6) solves

$$T_{\text{mrt},Tg} = \left(T_g^4 + \frac{\bar{h}_{c,g}}{\sigma_{\text{SB}} \cdot \varepsilon_g} \cdot (T_g - T_a) \right)^{0.25} \quad (7)$$

Outdoor forced convection dominates for $v_a \geq 0.03 \cdot (T_g - T_a)^{0.42}$ [38]. According to the similitude theory $\bar{h}_{c,g} = \kappa \cdot \overline{Nu} / L$. \overline{Nu} (dimensionless) is the mean Nusselt number, i.e., the ratio of mean convective $\bar{h}_{c,g}$ to conductive heat transfer κ ($\text{W}\cdot\text{m}^{-2}\cdot\text{K}^{-1}$) in the film layer, here at the boundary between the air and the globe's shell. L (m) is the characteristic length, for the sphere it is d_g . \overline{Nu} is additionally a function of v_a on the sphere and of air properties, namely kinematic viscosity, specific heat capacity, thermal conductivity and density that are usually summarized in the value 6.3 [8,22] for standard atmospheric conditions. Thus, the black globe equation for forced convection (6) reads

$$T_{\text{mrt},Tg,BG} \approx \left(T_g^4 + \frac{6.3}{\sigma_{\text{SB}} \cdot \varepsilon_g} \cdot \frac{v_a^{0.6}}{d_g^{0.4}} \cdot (T_g - T_a) \right)^{0.25} \quad (8)$$

2.5. Data

In order to realistically compare $T_{\text{mrt},r,6\text{-Dir}}$ against $T_{\text{mrt},r,KMM}$, observations are required that cover in particular a sufficient number of solar altitudes and weather conditions. Such large amounts of observations are not available under all weather conditions for the 6-Dir instrument. Therefore, the fact is exploited that direct, diffuse and surface reflected SW and thermal LW irradiances onto tilted surfaces can readily be calculated based on (solar) geometry from standard meteorological irradiance measurements (see e.g., [32]). The sole exception in the transposition to tilted surfaces is the anisotropic fraction in E_D . No such measurement is available and, thus, has to be modeled. To this end, a three component treatment of sky diffuse irradiance is applied based on known values of E_D , E_G and γ_s . [23,25]. The circumsolar fraction f_{cs} is then treated like E_L , i.e., dependent on solar geometry. The small band of horizon brightness is added to the isotropic fraction in E_D . E_R is regarded as exclusively isotropic diffuse, like E_A and E_E . Hence, for an environment with no significant horizon limitations [33], the SW and LW flux densities on the vertical surfaces of the 6-Dir instrument can be derived from standard horizontal and beam irradiance measurements based on more or less exclusively geometric relations.

T_{mrt} is applied as input for the calculation of thermal indices that represent steady state thermophysiological values of a reference person. Because steady state is usually achieved within 2 h [7,40], hourly sums of irradiation are the appropriate radiant input to characterize the radiant conditions in the adaptation phase leading to steady state. Table 1 lists the radiant components and auxiliary quantities that are available in hourly resolution for the years 2006 and 2007 from WMO Baseline Solar Radiation Network (BSRN) sites [13]: Ny Alesund (NYA), Norway: 78.93° N, 11.95° E, 11 m MSL; Lerwick (LER), United Kingdom: 60.13° N, 1.18° W, 84 m MSL; Payerne (PAY), Switzerland: 46.82° N, 6.94° E, 491 m MSL, Sde Boqer (SBO), Israel: 30.91° N, 34.78° E, 500 m MSL. BSRN data offer the highest available accuracy [41]. All BSRN sites fulfill the conditions that they are free from immediate local effects such as pollution, heat island effects, local orography such as surface tilt and elevate horizon, and isolated atmospheric conditions such as local cloud developments [13].

Table 1. Available observed (■) and missing (—) irradiation data in hourly resolution; SYNOPs: daily start time (temporal resolution) end time; observed black globe (BG) temperatures including auxiliary quantities.

Component	NYA	LER	RWA	PAY	SBO
E_I	■	■	■	■	■
E_D	■	■	■	■	■
E_G	■	■	■	■	■
E_R	■	—	■	■	—
E_A	■	■	■	■	■
E_E	■	—	■	■	—
SYNOP	06(3)18	00(1)23	00(1)23	00(3)21	06+18
BG: $T_g + t_a, v_a$	—	—	■	—	—

The missing E_R for LER and SBO is replaced by assuming $\rho_s = 0.2$. The missing E_E for both sites is modeled using a Bowen approach in solving the energy balance at the earth’s surface [12]. The latter requires auxiliary quantities from synoptic meteorological observations (SYNOP) that are only available in very limited quantities for SBO. Because these are limited to 06 and 18 UTC, radiant components for high solar altitudes (noon) cannot be modeled.

For the years 2001 to 2003, hourly radiant components for Rostock-Warnemuende (RWA), Germany: 54.18° N, 12.08° E, 4 m MSL are also available (Table 1). Their accuracy is in line with long-term measurements of national meteorological services [41]. The measuring field is located in the dunes bordering the Baltic Sea. Here, the SW E_R is measured accounting for the higher albedo of the dune sand and the LW components E_A and E_E are measured based on Schulze pyrrometers. Compared to pyrogeometers, the measurements should show approximately identical means, but the individual values are characterized by a slightly increased variance [42]. The SW components of the upper half space are measured at roof height of the nearby building of the meteorological site.

At RWA, T_g from a black globe thermometer is also available, as are t_a and v_a taken at the height of the black globe. t_g and t_a are quantified with copper-constantan thermocouples according to the standard TGL 32603/2 [43], where t_a is additionally controlled against the air temperature measured with a standard PT-100 resistance thermometer [44]. v_a is taken with a Thies opto-electric anemometer, start-up-speed 0.3 (m/s). 10 min averages in UTC are accumulated to hourly means in true solar time.

2.6. Assessment Methodology and Reference

ISO 7726 [8] specifies the accuracy requirements for measuring methods based on the extent of the thermal annoyance being assessed. The more stringent requirements are for methods that relate to measurements carried out in moderate environments approaching comfort conditions, the less stringent are for environments subject to greater thermal stress. The latter may be considered for outdoor applications. Slightly simplified and thereby fractionally intensified in the extremes, the accuracy requirements of ISO 7726 [8] in T_{mrt} are ± 2 K for comfort and ± 5 K for thermal stress. Subsequently, methods for the calculation of T_{mrt} are tested against a reference method. It is assessed whether the differences in T_{mrt} against the reference is within the thresholds ± 2 K or ± 5 K. In order to comply with the ISO standard, the maximum error probability (α_{2K}, α_{5K}) has to be less than 5%. Further statistical values that are provided are the bias (K) as the mean of the differences, the root mean square error RMSE (K), and for linear regressions intercept (a) and slope (b), the coefficient of determination (R^2) and the standard error (SE). SE is a measure of scattering of the sample points related to the regression value.

The assessment methodology requires a reference method. All three methods can be traced to proposals of ISO 7726 [8] for the measurement/calculation of T_{mrt} :

- $T_{mrt,r,KMM}$: Calculation from the temperature of the surrounding surfaces (Equation (1)) in the form for outdoor use [1,12]. f_p (Equation (2)) parameterized from diagrams [6]. This parameterization is

confirmed by more recent measurements (Figure 1) [11]. In the extended form $T_{mrt,r,KMM}$ accounts for f_{cs} . $T_{mrt,r,KMM}$ can be calculated based on standard meteorological radiant measurements.

- $T_{mrt,r,6-Dir}$: Calculation from plane radiant temperatures [8] in the form for outdoor use [1,15]. The reference person is slightly simplified by a rectangular solid (Figure 1). The method implicitly accounts for f_{cs} , because measured irradiances incident on vertical planes are used that depend on the azimuth of a plane relative to the azimuth of the solar disk. Variations in the accuracy of the instrument have been observed [45–47].
- $T_{mrt,Tg,BG}$: Derived based on measured t_g , t_a and v_a (passive radiometry). ISO 7726 qualifies $T_{mrt,Tg,BG}$ to be an approximation due to the difference in shape between a person and a globe. The vertical component in E_I will be over-estimated in relation to that received by a standing person. The SW absorptivity significantly differs from that of the outer surface of a clothed person.

$T_{mrt,r,KMM}$ is adopted as the reference because it applies directly observable radiant components (subscript: r) that are used as standard in meteorology. In $T_{mrt,r,6-Dir}$ it is implicitly accounted for the circumsolar fraction of E_D . However, this advantage cannot be completely used, because the data must be modeled (Section 2.5). Furthermore, f_p for $T_{mrt,r,KMM}$ is derived from precise measurements of the real human bodies [6,10,11], while in $T_{mrt,r,6-Dir}$ the shape of the human body is slightly simplified to a rectangular solid.

3. Results

3.1. Six-Direction Measurements

Variations in the accuracy of 6-Dir measurements have been observed [45–47]. Because the 6-Dir method assumes the subject to be a rectangular solid, its vertical cross-section for unidirectional SW irradiance is a function of the difference in azimuth between the solar azimuth and the azimuth angle of one of the vertical surfaces (ΔA_{az} (degrees)) that are irradiated by the unidirectional fraction $(1 - Df)$ in E_G [30]. $Df = (1 - f_{cs}) \cdot E_D/E_G$ is the isotropic diffuse fraction. The unidirectional cross-section is smallest for $\Delta A_{az} = 0^\circ$ because there is only one sunlit vertical surface, and greatest for 45° . In contrast, the vertical cross-section of a circular cylinder is azimuthally independent. Figure 1 presents the projected area factor of a cylinder that has the same relation of the cylindrical surface area and the surface area of the two parallel planes as the total vertical to the horizontal areas of the rectangular solid. Compared to that cylinder, the rectangular solid deviates in received irradiance due to the anisotropic fraction in SW irradiance (ΔE_{an} (W/m^2)) indicated by:

$$\Delta E_{an} = (1 - Df) \cdot E_G \cdot \cot(\gamma_s) \cdot \left(\sqrt{1 + \sin(2 \cdot \Delta A_{az})} - 1.273 \right) \tag{9}$$

Because they are based on the same measured radiant fluxes, differences in $T_{mrt,r,6-Dir}$ and $T_{mrt,r,KMM}$ can only arise from the anisotropic radiant parameters and the slightly differing f_p (see Figure 1). Therefore, the evaluation of differences is restricted to daylight hours.

Figure 2a,b summarize the results for two azimuthal orientations of the 6-Dir instrument, where (a) assumes a measuring routine in which one of the vertical surfaces is set facing south, and (b) assumes that one of the vertical surfaces faces the solar azimuth. The reference accounts for variable f_{cs} , despite the fact that it has to be modelled based on measurements. Figure 2c shows the effect of a reference that does not account for the circumsolar fraction in E_D , i.e., in Equation (3) $f_{cs} = 0$, as was originally suggested [12]. Figure 2d enables Figure 2a,b to be compared to a circular cylinder.

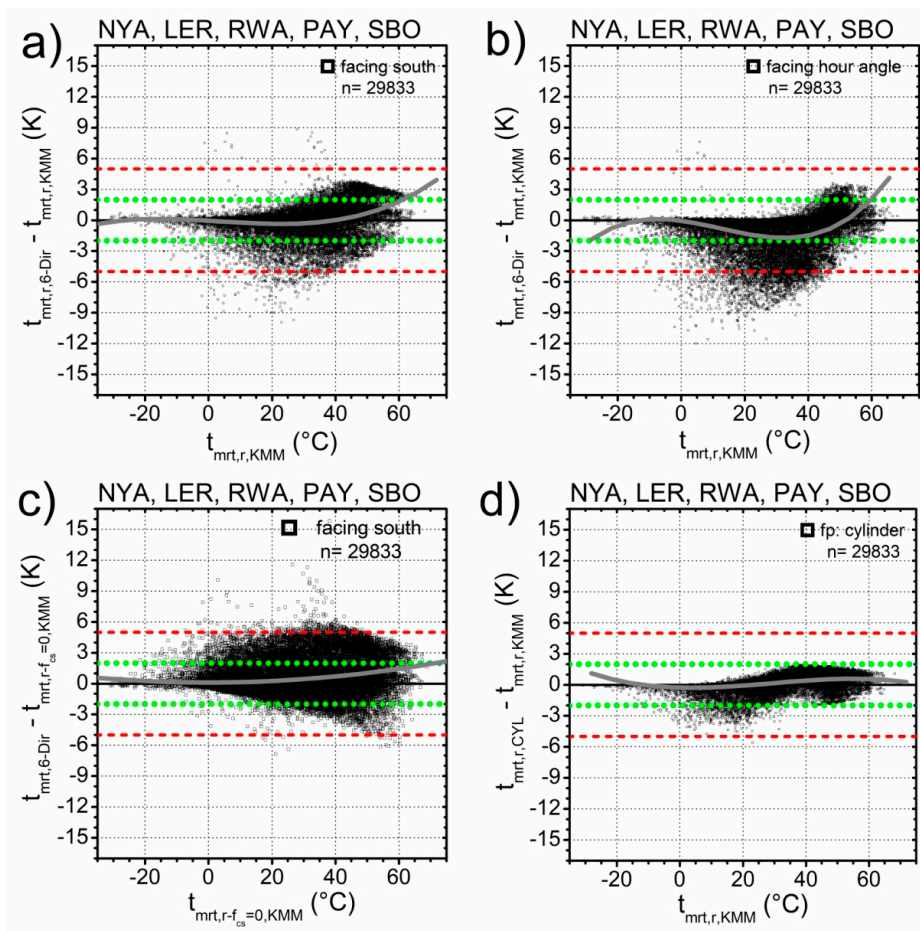


Figure 2. Difference of 6-Dir instrument and cylinder to the reference $t_{mrt,r,KMM}$. Green dotted lines delimit the ISO comfort class ± 2 (K), red dashed lines the stress class ± 5 (K). $t_{mrt,r,KMM}$ accounts for variable f_{cs} : (a) the 6-Dir is set to face south; (b) the 6-Dir moves to face the solar disk; (c) 6-Dir faces south, however, $T_{mrt,r,KMM}$ does not account for anisotropy in E_D , i.e., $f_{cs} = 0$; (d) for a cylinder with the same relation of barrel and covers, and $t_{mrt,r,KMM}$ accounts for variable f_{cs} .

All orientations and assumptions remain within the ISO 7726 thresholds for thermal stress of ± 5 (K) (Table 2). However, the comfort threshold of ± 2 (K) is met only by the cylinder and with an error probability $\leq 1.3\%$ by the 6-Dir instrument facing south. Because of its azimuthal dependence, the scattering in the t_{mrt} differences is stronger for the rectangular solid than for the cylinder (Figure 2a,d). It significantly increases if the reference does not account for variable f_{cs} (Figure 2c versus Figure 2a). If a measuring routine is assumed in which one of the vertical surfaces faces the solar azimuth (Figure 2b), this results in a significant negative bias of approx. -1 (K), because only one of the vertical surfaces is sunlit with unidirectional irradiance (Table 2). Thus, the bias due to the azimuthal error approaches zero if the instrument has a fixed orientation. The statistics of Table 2 include the data of the sites LER and SBO where the upward SW and LW components are modeled. The statistical results do not differ if the data of the two sites are not accounted for.

Table 2. Six-directional (6-Dir) instrument and cylinder: Statistics for the difference $T_{mrt,r,6-Dir} - T_{mrt,r,KMM}$ and error probability (α_{2K} , α_{5K}) for compliance with ISO 7726; $n = 29,833$ daylight hours.

	6-Dir Instrument	Bias (K)	RMSE (K)	α_{2K} (%)	α_{5K} (%)
$f_{cs} = \text{var}$	facing south	-0.08	1.39	1.3	<0.1
$f_{cs} = \text{var}$	facing hour angle	-0.97	2.09	9.8	<0.1
$f_{cs} = 0$	facing south	-0.77	2.00	18.3	0.1
$f_{cs} = \text{var}$	cylinder	-0.05	0.74	<0.1	<0.1

The third order polynomials in Figure 2 prove the impact of the more greatly simplified assumptions concerning the human body compared to f_p of Equation (2). Especially for increased $T_{mrt,r,KMM}$, the differences tend toward values greater than zero. Here, the higher values are frequently combined with increased γ_s and, thus, with a higher probability of anisotropic SW irradiances. The upper surface of the rectangular solid as well as the cover of the cylinder represents head and shoulder girdle of a human less precisely than Fanger’s f_p . As a consequence of the azimuthally dependent conditions of irradiance, the RMSE of the differences is almost double that in the rectangular solid compared to the cylinder (Table 2). In contrast, standard radiation measurements apply horizontal receivers that are by definition azimuthally independent. This gives additional support to the selection of $T_{mrt,r,KMM}$ as the reference.

Figure 3 highlights the effect of circumsolar anisotropy in E_D , $f_{cs} = \text{variable}$, for determining $T_{mrt,r,KMM}$ by comparing it with the case in which it is neglected, $f_{cs} = 0$ [12]. In the extremes, $T_{mrt,r-fcs=var,KMM}$ can deviate from $T_{mrt,r-fcs=0,KMM}$ by approx. +5 (K) for solar altitudes γ_s close to the horizon and by approx. -7 (K) for the maximal γ_s of about 68 (degrees) within the data (due to SYNOPs only for 06 and 18 UTC at SBO (Table 1), higher solar elevations using modeled components are not attainable). Because the reference person is standing, the area projection factor f_p for unidirectional SW irradiance increases with decreasing γ_s (Figure 1) and provides evidence for the positive deviations. For a given γ_s , the scattering in the differences arises from variable cloudiness due to the decreasing anisotropy effect with increasing cloud levels. At $\gamma_s \approx 32$ (degrees), the optical air mass for the direct solar beam equals the mean value of the isotropic diffuse fraction and, thus, the anisotropic part in E_D contributes to $T_{mrt,r,KMM}$ by the same amount as if it were treated as isotropic. Because the optical air mass decreases in proportion to the increasing γ_s , there is a lower probability of the direct solar beam being scattered in its transfer to the earth’s surface. Hence, for high γ_s the differences tend towards a higher absolute value.

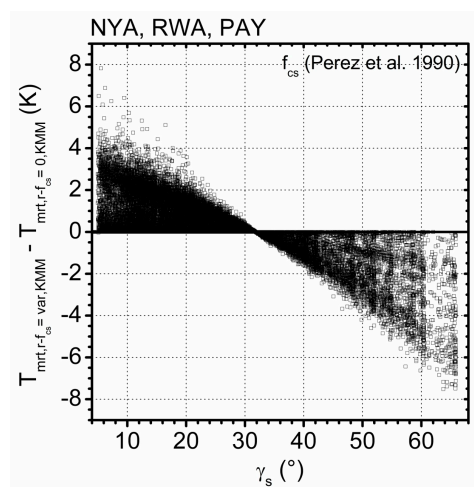


Figure 3. Solar altitude difference in $T_{mrt,r-fcs=var,KMM}$, that accounts for circumsolar anisotropy in diffuse irradiance, to the case $T_{mrt,r-fcs=0,KMM}$, that disregards the anisotropy effect.

3.2. Black Globe Thermometer

A total of 25311 hourly mean values of measured T_g of a black globe is available for Warnemuende (RWA). They also include hours with precipitation that may impact T_g due to evaporative effects etc. Based on hourly synoptic observations, all T_g means are excluded that, in the present weather or within the past few hours, showed WMO-FM12 code numbers [48] greater than 10, i.e., cases with drizzle, rain, snow, thunderstorm etc. Furthermore, hours are excluded with an air speed at the height of the globe thermometer which is less than that of forced convection and/or with a difference in the air temperature registered by the thermocouples and the PT100 thermometer that exceeds 2 (K). Thus, 9191 values remain that are all covered by measured radiant components required to calculate $T_{mrt,r,KMM}$.

t_g is not a thermodynamic property [49] but a measure of the complex radiant and convective effects of the environment on the black globe. Figure 4 examines some of them and their implications for the derived $T_{mrt,Tg,BG}$. It is also closely related to frequent attempts to predict t_g based on standard meteorological measurements [34,49–54]. Figure 4a relates t_g (°C) to t_a (°C), where t_g is split into three bins of radiant conditions: (i) at nighttime, i.e., sun is below the horizon, at daytime dependent on the value of E_I : (ii) cloudy, i.e., $E_I < 120$ (W/m²), no sunshine according to WMO [14], and (iii) sunny, i.e., $E_I \geq 120$ (W/m²).

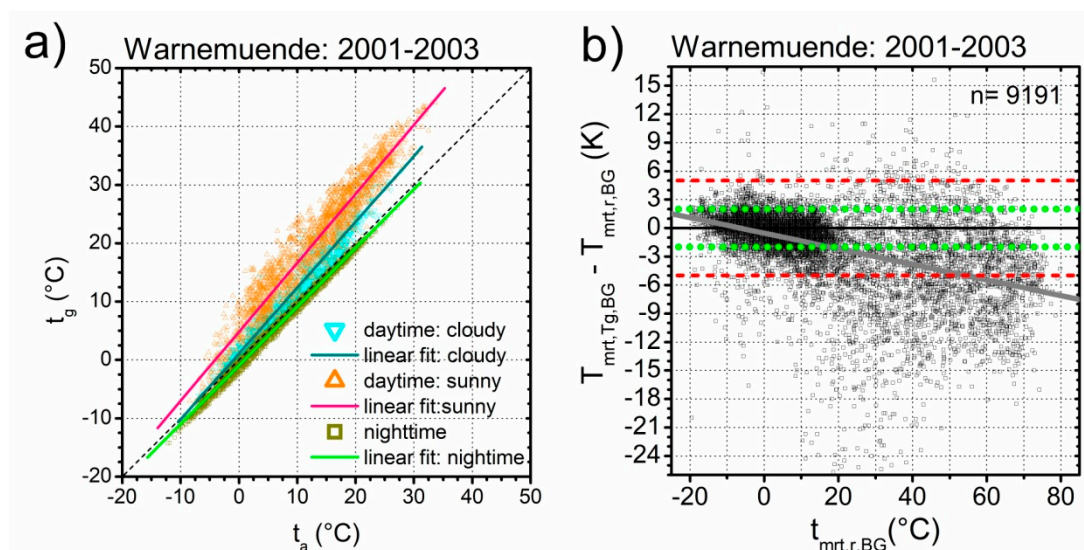


Figure 4. (a) Globe temperature t_g versus air temperature t_a , (b) difference $T_{mrt,Tg,BG}$ (K) derived from measured t_g of a black globe instrument (BG) minus $T_{mrt,r,BG}$ (K) calculated from measured shortwave (SW) and longwave (LW) irradiation for the assumption of a black globe versus $t_{mrt,r,BG}$ (°C), where green dotted lines delimit the ISO comfort class ± 2 (K) and red dashed lines the stress class ± 5 (K).

At nighttime the radiant heat transfer is limited to E_A and E_E , the thermal spectral band. Then, t_a and t_g are closely and linearly regressed with the slope of the regression line close to unit (Table 3). The difference $t_g - t_a$ is negatively biased by -0.9 (K), which provides evidence that, in most cases, it is the lower half space that in balance transfers radiant heat to the atmospheric environment. The scattering of the data can be attributed predominately to the varying v_a that is responsible for the convective heat loss.

Table 3. Black globe instrument (BG): linear regression of t_g (C) versus t_a (C).

Data Fraction	Test Value	Reference	Bias (K)	RMSE (K)	a (°C)	b	SE (K)	R ²
nighttime	t_g	t_a	−0.90	1.09	−0.93	1.01	0.62	0.99
daytime: cloudy	t_g	t_a	+2.20	3.05	+1.09	1.13	1.94	0.94
daytime: sunny	t_g	t_a	+7.11	7.83	+4.81	1.18	2.91	0.92

During the daytime, SW irradiation transfers heat onto the black globe, and the absorbed SW energy very often results in an increased t_g , the amount of which depends on the SW intensity. At daytime in cloudy hours the sky is most frequently overcast, i.e., E_D accounts for the largest share in E_G . Compared to nighttime, the absorbed SW irradiance gives reason that the bias turns to positive and that the slope of the regression increases to 1.13. Compared to nighttime, the standard error is increased by a factor three and amounts to 1.9 (K). In the sunny hours, there is stronger SW heat transfer onto the black globe, the slope increases to 1.18, at +7.1 (K) the regression has a markedly positive bias and the standard error increases to +2.9 (K) (Table 3). The scattering in the data is significantly increased compared to the nighttime because v_a impacts on the convection, but t_{mrt} also varies.

In the next step, a $T_{mrt,r,BG}$ is simulated for a black globe based on measured radiant components. Because of the sphere’s simple geometry, its area projection factor is $f_p = 0.25$ and independent of γ_s (Figure 1). Then, $T_{mrt,r,BG}$ can be derived by applying Equation (3), assuming $\alpha_{sw,Sk} = 0.95$ and $\varepsilon_{sw,Sk} = \varepsilon_g = 0.95$ [8]. Because it is based in this case on measured radiant quantities, $T_{mrt,r,BG}$ is assumed as the reference. By highlighting the difference to $T_{mrt,r,BG}$, Figure 4b shows that $T_{mrt,Tg,BG}$ significantly underestimates $T_{mrt,rKMM}$, bias −1.9 (K), which in this study is defined as reference (Table 4). The ISO 7726 [8] requirements for neither the comfort class nor thermal stress are met. The differences scatter significantly, especially for values of $T_{mrt,r,BG}$ greater than approx. +20 (°C).

Table 4. Statistics for the difference T_{mrt} from a globe minus T_{mrt} of a reference based on measured radiant components. First section: comparison of values derived from BG measurements versus simulated BG values; second section: simulated values for a black (BG) and a gray globe (GG) versus the KMM reference; third section: measured BG values versus the KMM reference for different data fractions. Error probabilities (α_{2K} , α_{5K}) for compliance with ISO 7726 [8].

Data Fraction	Test Value	Reference	Bias (K)	RMSE (K)	α_{2K} %	α_{5K} %
total	$T_{mrt,Tg,BG}$	$T_{mrt,r,BG}$	−1.90	4.74	47.8	7.6
total	$T_{mrt,r,BG}$	$T_{mrt,r,KMM}$	+2.77	5.18	47.0	7.1
total	$T_{mrt,r,GG}$	$T_{mrt,r,KMM}$	0.00	1.27	<0.1	<0.1
120 < $E_I \leq 600$ (W/m ²)	$T_{mrt,r,GG}$	$T_{mrt,r,KMM}$	−0.61	2.04	24.4	0.4
$E_I > 600$ (W/m ²)	$T_{mrt,r,GG}$	$T_{mrt,r,KMM}$	+0.61	3.16	45.2	6.0
total	$T_{mrt,Tg,BG}$	$T_{mrt,r,KMM}$	+0.86	4.85	49.5	8.8
nighttime	$T_{mrt,Tg,BG}$	$T_{mrt,r,KMM}$	−0.27	1.89	9.3	<0.1
daytime: cloudy	$T_{mrt,Tg,BG}$	$T_{mrt,r,KMM}$	+0.83	4.14	51.6	10.5
daytime: sunny	$T_{mrt,Tg,BG}$	$T_{mrt,r,KMM}$	+3.79	8.89	78.3	49.1
120 < $E_I \leq 600$ (W/m ²)	$T_{mrt,Tg,BG}$	$T_{mrt,r,KMM}$	+2.19	8.48	76.9	46.4
$E_I > 600$ (W/m ²)	$T_{mrt,Tg,BG}$	$T_{mrt,r,KMM}$	+5.87	9.41	79.8	52.3

Figure 5a relates the difference of simulated $T_{mrt,r,BG}$ to the reference $T_{mrt,r,KMM}$, where both $T_{mrt,r,BG}$ and $T_{mrt,r,KMM}$ use the same measured radiant components. The difference increases sharply with rising $T_{mrt,r,KMM}$ because the SW absorption of the black globe is $\alpha_{sw,Sk} = 0.95$ compared to KMM of $\alpha_{sw,Sk} = 0.70$. There is noticeable data scatter around their 4th order polynomial, SE = 1.68 (K), due to the fact that f_p of KMM is a function of γ_s while this is not the case for a sphere. Because of the enhanced SW absorption, the simulated $T_{mrt,r,BG}$ does not meet the ISO requirements, either for the comfort or for the stress class (Table 4).

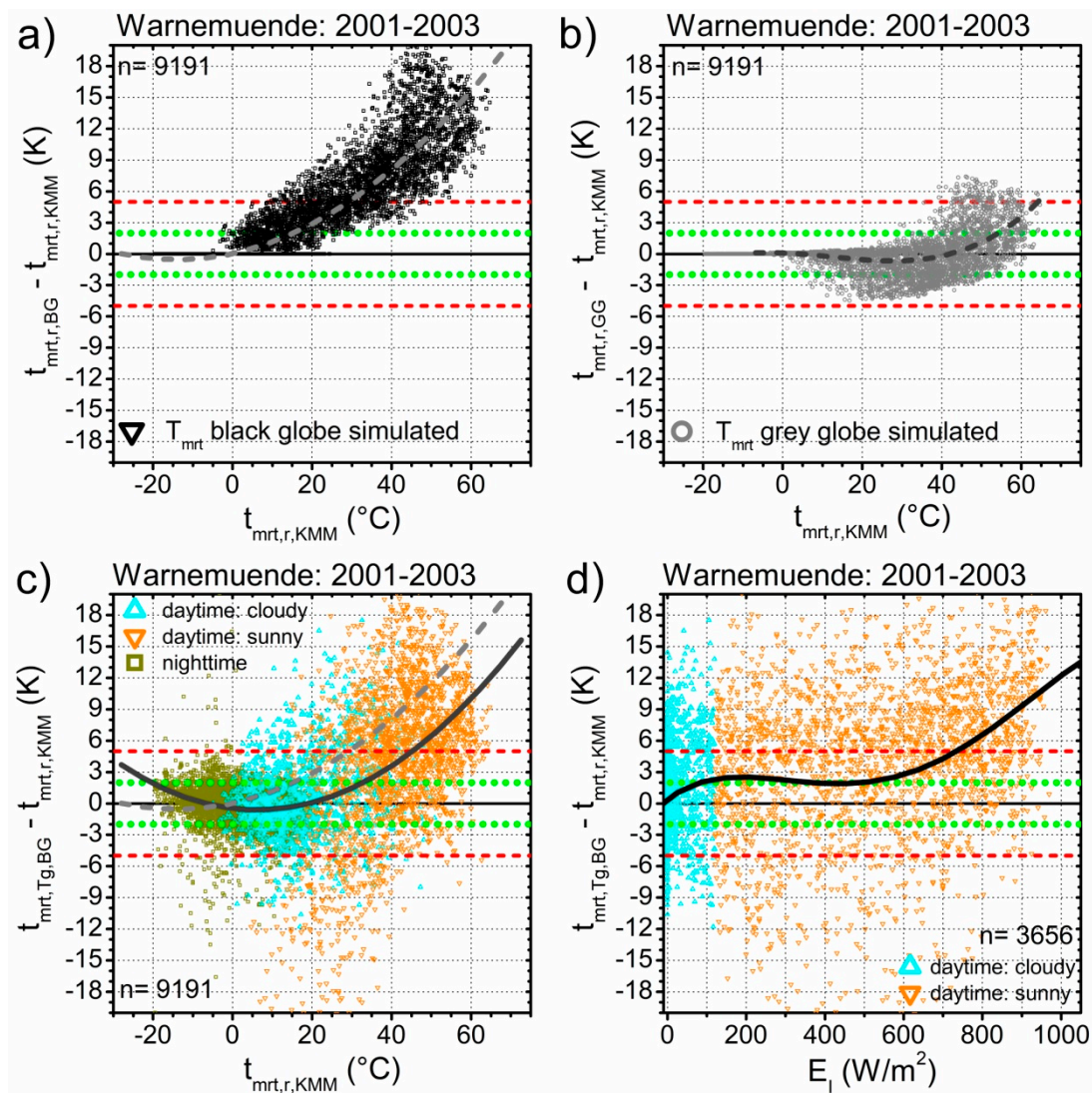


Figure 5. (a) Difference of simulated $T_{mrt,r,BG}$, $\alpha_{sw,Sk} = 0.95$, reference $T_{mrt,Tg,KMM}$ and a polynomial fit of the data given by the gray dashed line; (b) same as (a), however, $T_{mrt,r,GG}$ for a gray globe, $\alpha_{sw,Sk} = 0.70$; (c) difference of $T_{mrt,Tg,BG}$ as measured by a black globe and reference $T_{mrt,r,KMM}$ with polynomial fit, solid line, and the fit of (a), dashed gray line for comparison; (d) same as (c), however, restricted to daytime values and plotted over the direct irradiance E_I (W/m^2).

This alters when simulating a $T_{mrt,r,GG}$ for a gray globe (GG), assuming $\alpha_{sw,Sk} = 0.70$ as for KMM (Figure 5b, Table 4). The f_p -related scattering around the second-order polynomial remains unchanged; it is, however, somewhat reduced, $SE = 1.25$ (K). Because the simulated $T_{mrt,r,GG}$ complies with the ISO requirements both for the comfort and for the stress class (Table 4), it becomes evident that the f_p dependence is only of minor importance compared to the SW absorption. Time periods with summery more or less cloudless skies around noon may be characterized by $E_I > 600$ (W/m^2). Then, α_{5K} is just beyond compliance with the ISO 7726 stress class due to the differences in shape between a globe and a standing person (Table 4).

Figure 5c compares $T_{mrt,Tg,BG}$ to $T_{mrt,r,KMM}$: The scattering of the data values around their polynomial fits, $SE = 4.66$ (K), is considerably greater compared to $T_{mrt,r,BG}$ (Figure 5a), $SE = 1.68$ (K). In total, however, the values of the T_g -derived $T_{mrt,Tg,BG}$ are lower than those of $T_{mrt,r,BG}$. This fact is clearly demonstrated by the two polynomial fits, where the dashed line is the fit of Figure 5a. Overall, $T_{mrt,Tg,BG}$ does not comply with the ISO 7726 requirements, either for the comfort or for the

thermal stress class (Table 4). Splitting the data into nighttime values and the daytime data into cloudy and sunny components reveals that the ISO 7726 class for thermal stress is met at nighttime (Table 4). There is a slight bias in the data, -0.27 (K), RMSE = 1.89 (K). During the daytime, the data do not comply with the ISO 7726 requirements, there is a positive bias for cloudy conditions $+0.83$ (K), increasing to $+3.79$ (K) during sunny periods (Table 4). Thus, the daytime results of the globe instrument show significant shortcomings compared to those derived from active radiometry. These shortcomings are attributable to the SW irradiation E_G that covers the isotropic diffuse fraction of E_D and the unidirectional fraction E_I as well as the circumsolar part of E_D . Especially under sunny conditions and high radiant intensity the unidirectional fraction accounts for the largest share in E_G with ~ 75 – 85% . Thus, E_I is suitable to characterize conditions where the black globe thermometer is subject to strong asymmetric SW irradiation. Plotted over E_I , the daytime data of the difference $t_{\text{mrt},T_g,BG} - t_{\text{mrt},r,KMM}$ show a bias of $+2.2$ (K) for $120 < E_I \leq 600$ (W/m^2) due to the enhanced SW absorption of the black globe compared to KMM (Figure 5d, Table 4). Stronger asymmetric radiant conditions can be attributed to values of $E_I > 600$ (W/m^2). Here the bias rises sharply with increasing E_I (Table 4). For a gray globe that has the same radiant cross-section as the black globe but a reduced SW absorptance ($\alpha_{\text{sw},Sk} \sim 0.70$), the maximally absorbed energy from unidirectional irradiances may be reduced to approx. 600 (W/m^2) and the bias will be closer to zero. Because of the comparable amount of absorbed unidirectional radiant heat, it can be inferred from Figure 5d that the scattering in the data of a gray globe will be approximately the same as for the black globe in the region $E_I < 600$ (W/m^2), and, thus, significantly enhanced compared to $T_{\text{mrt},r,GG}$ (Figure 5b) and markedly too large to comply with the ISO 7726 stress class.

4. Discussion

At nighttime, $T_{\text{mrt},T_g,BG}$ remains within the ISO 7726 [8] thresholds for the stress class when applied as a measure for $T_{\text{mrt},r,KMM}$. During daytime, and especially in summery sunny conditions, there is a significant positive bias and, in particular, markedly greater scattering in the values so that the stress class thresholds are far exceeded. This provides additional evidence that the increased scattering is a typical outdoor problem of a black globe thermometer, and coincides with other findings (e.g., [55]). Under direct sun, the SW irradiance is strongly asymmetric; a temperature difference of up to 7 (K) in opposing areas of the inner surface has been measured [56]. Additionally, the wind field on the outer border of the sphere's film layer is not entirely uniform [57]. Therefore, the wind direction relative to the hot spot of direct irradiation can influence the overall convective cooling of the globe. This spatial relationship between the fields of irradiance and of wind is important for the internal convection. Both theoretically and in experiments, the internal flow and temperature fields become asymmetric [37,55,58]. Thus, under strong asymmetric irradiation the temperature at the sphere's center is unable to represent the average surface temperature of the globe thermometer system.

The black globe was originally introduced in order to measure radiant heat in relation to human comfort [17]. By chance, \overline{Nu} of the applied sphere with $d_g = 0.15$ (m) is identical to that of a naked recumbent man [57]. Based on the similitude theory, this diameter is fundamental when T_g is related to human comfort, i.e., T_g is closely correlated with the operative temperature. Nevertheless, in the case of the black globe, it has the disadvantage that its SW absorption is significantly higher than that of human skin/clothing and thus tends to overestimate T_{mrt} when applied to human thermophysiology [22]. In contrast to comfort, the diameter is not predetermined using the black globe as a passive radiometer in order to determine T_{mrt} [16]. According to Equation (8), smaller diameters will improve the convective heat loss but will demand more accurate measurements of air velocity and ambient temperature [8,22,59,60].

Rewriting the transient form of the globe's heat balance, Equation (6), in a linearized form allows, through temporal integration, the time constant of the instrument (τ (s)) to be determined for a stepwise change [38]: $(Q_{\text{Ir}} - Q_{\text{c}})_{\text{outer}} = \varepsilon_g \bar{h}_{r,g} \cdot (T_{\text{mrt}} - T_g) - \bar{h}_{c,g} \cdot (T_g - T_a) = -\rho \cdot c \cdot \delta \cdot dT/dt$, where $\bar{h}_{r,g} \approx 4 \cdot \sigma_{\text{SB}} \cdot ((T_{\text{mrt}} + T_g)/2)^3$ ($\text{W} \cdot \text{m}^{-2} \cdot \text{K}^{-1}$) is the mean radiant heat transfer coefficient [61]. τ

represents the time in which T_g reduces by 63.2% to the value of equilibrium. Within the response time, i.e., six to seven times τ , T_g has balanced out. Restricted to the heat exchange between the globe's shell and the environment, τ is a function of $\bar{h}_{c,g}$. This depends, among other things, on the globe's geometry and its material characteristics, as well as on $\bar{h}_{r,g}$. τ strongly decreases as the result of increasing $\bar{h}_{c,g}$ that is a function of v_a . Outdoors, v_a is greater than in typical indoor conditions at $v_a \leq 0.2$ (m/s). At RWA, where the measuring field is located in the dunes bordering the Baltic Sea, the mean of all records is $v_a = 2.34$ (m/s), the median 1.8 (m/s). In typical summery conditions, $t_a = 18.4$ ($^{\circ}\text{C}$), $v_a = 2.6$ (m/s), $t_{\text{mrt},T_g,\text{BG}} = 25.8$ ($^{\circ}\text{C}$), the calculated response time is 5.25 (min) and is lower than for the same conditions by a factor of ~ 3 , yet $v_a = 0.20$ (m/s). However, this does not take into account the heat conductivity of the shell's material and especially not the radiant properties of the inner surface and the mass of the thermometer's bulb which also affect the time constant of the instrument. The mass of the applied thermocouple is small, the emissivity of the oxidized copper inside the sphere is, at ~ 0.4 , relatively low and there is only free convection. Hence, overall the instrument's response time will be increased, but should not exceed observed values of about 10 min for outdoor air velocities of ~ 2 (m/s) [62]. Instruments have been constructed with a fan inside the sphere for forced convection in order to improve their response time [36,63]. However, they have not achieved greater acceptance.

Outdoors the environment is not in a steady state, i.e., the globe is impacted by short-term fluctuations, e.g., by wind gusts and brief cloud shadows in the case of broken cloud coverage, but usually this is only temporary. Hence, the hourly averages of measured T_g will rarely represent a steady state in the globe thermometer. Over the course of the day, they may include a time shift compared to the radiances, however these can be regarded as more or less insignificant.

Indoor black globe systems have been introduced, the shell of which consists of a table-tennis ball (acrylic), diameter ~ 0.04 (m), that is painted matt black. Their purpose is to achieve a quicker response time and lower instrument costs [64,65]. As a result of these reported advantages, such black globe instruments are now also being used outdoors [20,21]. However, under the strong asymmetric SW irradiation found outdoors, the heat conductivity of acrylic can no longer be ignored in terms of the heat balance of the system because it is lower than that of copper by a factor of ~ 1000 . This may outweigh the reduced response time due to the lower mass density of acrylic compared to copper, and the reduced diameter. It is not recommended to use table-tennis balls outdoors as black globe thermometers in order to determine T_{mrt} because they yield unpredictable errors in the measurements [37,55].

The wet-bulb-globe-temperature (WBGT) index [18] is an index of thermal stress and has been adopted as standard ISO 7243 [19]. WBGT has the advantage that it can also be evaluated directly outdoors by taking readings of its three input components: the natural wet bulb temperature (t_{nw} ($^{\circ}\text{C}$)) as well as t_a ($^{\circ}\text{C}$) and t_g ($^{\circ}\text{C}$). They are summarized in the weighted average $\text{WBGT} = 0.7 \cdot t_{\text{nw}} + 0.1 \cdot t_a + 0.2 \cdot t_g$. The weights are empirically determined by linking them with heat casualties and work-rest cycles needed to prevent thermal strain on humans in the workplace [3,18,66,67]. T_{mrt} is not explicitly required as WBGT input. Hence, uncertainties in t_g as found in this study are irrelevant for the accuracy of the WBGT index because they are accounted for in the weights. However, when the diameter of the globe used differs from the standard 0.15 (m), the measured t_g value has to be adapted to the standard configuration [35,50,68]. Here the algorithm is based on v_a and the magnitude of the difference $t_g - t_a$ [62]. It is difficult to measure t_{nw} and t_g , which are not thermodynamic properties [49]. Thus, measures have been undertaken in order to derive them from environmental data. In the case of t_g , this can be achieved by solving Equation (7) for T_g . The required input T_{mrt} may be derived, assuming that it is a linear function of t_a [51,52], i.e., radiant flux densities are only estimated. In more recent approaches, T_{mrt} is explicitly derived from readily available standard meteorological data that include the above-mentioned data from active radiometry (e.g., [24,34,53,54,67]). Here, $T_{\text{mrt},r,\text{BG}}$ can be calculated for a black globe by means of Equation (3) using $f_p = 0.25$ and $\alpha_{\text{sw},\text{Sk}} = 0.95$. Then, Equation (7) is solved for T_g by iteration or by using empirical/polynomial methods. As this study found, it is advantageous for such empirical approaches to differentiate during the daytime between conditions in which the black globe is sunlit or is shaded [50] and to address separately

nighttime data that are more closely linked to t_a (Figure 4a) [54,69]. From the correlation of modeled against observed t_g [49,50,54] and from the difference $T_{\text{mrt,Tg,BG}} - T_{\text{mrt,r,KMM}}$ as a function of t_g [70], it is apparent that the observed t_g exhibits the same problem as seen here, especially under sunny conditions (see Figure 4a,b, Table 4).

With the exception of E_I , observed standard radiant components refer to horizontally mounted receivers. These measurements have the advantage that they do not depend on the solar azimuth. In contrast, the irradiance on the vertically mounted receivers of the 6-Dir instrument depends on the solar azimuth and the measured values consist of radiant components incident from the lower and the upper half space. If the irradiance incident from the ground can be regarded as Lambertian equivalent, which is generally the case, then the sum of E_I and the circumsolar fraction of E_D can be derived from the irradiance difference of the sunlit and the shaded receivers accounting for γ_s [47]. This implies, however, an environment free of significant horizon limitations [33]. The 6-Dir instrument is mainly intended for measurements in micro-structured urban environments. In, e.g., a narrow street canyon with the measuring site positioned closer to a building, the albedo of the building surfaces will significantly affect the measured diffuse SW irradiation, and the precondition for the method is violated.

In an urban environment, standard active radiometry combined with Equation (3) can also be used in order to derive T_{mrt} for a human bioclimatological assessment. Deploying a sun tracker to measure E_I or E_D may be costly. An alternative could be to deploy a rotating shadow band irradiator. After correction for its deviation from the Lambertian response and for its nonuniform spectral response, the instrument delivers both E_G and E_D in moderate to good quality, which allows E_I to be inferred [71,72]. Furthermore, the input values for Equation (3) may be measured at roof level, i.e., without horizon limitations [33], or taken from a nearby meteorological site. Then, the derived $T_{\text{mrt,r,KMM}}$ is valid for the sky fraction seen from the point of assessment, the sky view factor, and the observed radiation flux densities can serve as a force in modeling the radiation transfer within the complex urban environment [21,73–75]. The observations of irradiation at meteorological sites frequently do not include all the components required to derive $T_{\text{mrt,r,KMM}}$. It has been shown that it is possible to calculate it with the required accuracy for the ISO 7726 thermal stress class if E_G and a synoptic observation are available to serve as the base in order to model the missing radiant components [30,76].

As part of the model output, Numerical Weather Prediction (NWP) usually delivers in hourly resolution not only t_a , e_a (2 m above ground) and v_a (10 m above ground) but also gridded data of irradiation sums starting with the initialized analysis. Based on the example of the Deutscher Wetterdienst (DWD), E_G , E_D , and the LW irradiation balance $E_A - E_E$ may be available. The latter can be broken down using the forecast temperature of the ground surface or of the snow/ice surface, and converted using the Stefan–Boltzmann law to E_E . The SW ground-reflected irradiation E_R is derivable using the predicted ground albedo that varies over time, in particular due to snow cover or sea ice. Then, in NWP postprocessing, all input parameters are available to derive not only $T_{\text{mrt,r,KMM}}$ via Equation (3) but also thermal indices as a basis for forecasting the spatial and temporal development of thermal health hazards (see e.g., [77]). Furthermore, test reference years derived from gridded high resolution datasets can also be helpful in the context of planning and health issues [78,79].

5. Conclusions

Among the required input parameters for rational thermal indices, T_{mrt} is the most complex. The quality of these indices and of the derived thermal assessment of the environment depends on the quality of the input. The requirements for T_{mrt} are specified by ISO 7726.

Based on active radiometry T_{mrt} accounts for the absorbed radiation from both the SW and LW spectral bands. Most of the radiant components are isotropic. Restricted to the SW band there are, however, also unidirectional irradiances: E_I and under clear or partly obstructed skies a significant circumsolar fraction f_{cs} in E_D . f_{cs} significantly impacts T_{mrt} with noticeably reduced values for high

solar altitudes and increased for low elevations. Accounting for f_{cs} is essential for the accuracy of T_{mrt} . An extension to an existing algorithm is provided in order to include f_{cs} into the T_{mrt} calculation. We applied Fanger's area projection factor f_p , which is standard in determining the radiant cross-section of a person for unidirectional irradiance, because it is precisely aligned with measurements.

The method KMM processes radiant flux densities measured with receivers that are horizontally mounted. Such measurements are readily available from standard meteorologically radiant observations. E_I and f_{cs} can be traced to them. A parameterization of f_p is applied that is confirmed by more recent measurements. Hence, KMM serves as reference in order to study the accuracy of the other methods.

The 6-Dir instrument posits the human as a rectangular solid. The radiant flux densities incident on the vertical planes are provided by vertically mounted receivers. The contribution of the unidirectional SW fraction on the vertical planes depends to a certain degree on the difference in azimuth angle between a plane and the solar disk. However, the produced scattering remains in the frame of the ISO 7726 comfort class. Additionally, $T_{mrt,r,6-Dir}$ is in the second order, also varied due to the simpler geometry compared to a precisely aligned human subject. The measured fluxes on the vertical planes contain the impact of f_{cs} , an advantage of the method. Measurements on vertical planes are rarely available, i.e., they are not standard and are elaborate and expensive.

$T_{mrt,Tg,BG}$ is derived by solving the energy balance equation of the black globe thermometer. At nighttime, a $T_{mrt,Tg,BG}$ can be derived that complies with the ISO 7726 stress class. During daytime, $T_{mrt,Tg,BG}$ basically yields larger values than $T_{mrt,r,KMM}$ due to its significantly increased SW absorption. An effect of secondary importance is that a globe is less appropriate for representing a standing body posture. Sunny summer conditions are linked to strong asymmetric SW irradiation. This results in strong scattering in the measured T_g and derived $T_{mrt,Tg,BG}$. Hence, outdoors in sunny conditions it is impossible to derive a T_{mrt} value of sufficient accuracy that could serve as input for the rational thermal indices. Also measurements with a gray globe under stronger asymmetric radiant conditions will not comply with the ISO 7726 stress class due to basic deficits of the globe thermometer.

Henceforth, $T_{mrt,r,KMM}$ should serve as a reference in the scope of human biometeorology. It can be derived not only from standard, meteorologically observed radiant flux densities but also from the relevant NWP output and from partially modeled components that fill in for missing observed fluxes.

Author Contributions: Conceptualization, H.S. and A.M.; methodology, H.S.; software, H.S.; validation, H.S.; formal analysis, H.S.; investigation, H.S.; resources, H.S.; data curation, H.S.; writing—original draft preparation, H.S.; writing—review and editing, H.S. and A.M.; visualization, H.S.; supervision, A.M.; All authors have read and agreed to the published version of the manuscript.

Funding: This research received no external funding.

Acknowledgments: The WMO Baseline Network (BSRN) at ETH Zürich granted Weihs, University of Natural Resources and Life Sciences, Vienna, access to the radiation data. This study constitutes one of a range of purposes for which the data were retrieved. We would like to thank the following for the radiation measurements: M. Maturilli (Alfred-Wegener-Institut, Bremerhaven) as well as J.B. Orbak (Norwegian Polar Institute, Longyearbyen) for the data of Ny Alesund, Norway, P. Fishwick (UK Met Office, Lerwick) for Lerwick/Shetland, United Kingdom, L. Vuilleumier (MeteoSwiss, Payerne) for Payerne, Switzerland, and A. Zangvil (Institute for Desert Research) for Sde Boqer, Israel.

Conflicts of Interest: The authors declare no conflict of interest.

List of Essential Symbols

Symbol	Unit	Description
Df	-	isotropic diffuse fraction of E_D
d_g	m	diameter of the globe's shell
e_a	hPa	water vapor pressure
E_A	W/m ²	long-wave downward radiant flux density (atmospheric)
E_E	W/m ²	long-wave upward radiant flux density (earth surface)
E_D	W/m ²	short-wave downward diffuse radiant flux density

E_G	W/m^2	short-wave downward global radiant flux density
E_I	W/m^2	short-wave downward direct radiant flux density
E_R	W/m^2	short-wave upward surface reflected radiant flux density
f_a	-	angle factor for isotropic irradiances, horizon unobstructed
f_{cs}	-	anisotropic circumsolar fraction in E_D
f_p	-	projected area factor
$\bar{h}_{c,g}$	$W \cdot m^{-2} \cdot K^{-1}$	convective heat transfer coefficient averaged over the globe thermometer's surface
$\bar{h}_{r,g}$	$W \cdot m^{-2} \cdot K^{-1}$	radiant heat transfer coefficient averaged over the globe thermometer's surface
\overline{Nu}	-	mean Nusselt number of the globe thermometer
S_r	W/m^2	radiant energy absorbed by the 6-direction instrument
t_a, T_a	$^{\circ}C, K$	ambient temperature
t_g, T_g	$^{\circ}C, K$	globe temperature
t_{mrt}, T_{mrt}	$^{\circ}C, K$	mean radiant temperature
$T_{mrt,r,6-Dir}$	K	T_{mrt} derived from radiant fluxes measured with the 6-direction instrument
$T_{mrt,r,BG}$	K	simulated T_{mrt} of a black globe applying measured radiant fluxes and Equation (3) with $f_p = 0.25$ and $\alpha_{sw,Sk} = 0.95$
$T_{mrt,r,GG}$	K	simulated T_{mrt} of a gray globe applying measured radiant fluxes and Equation (3) with $f_p = 0.25$ and $\alpha_{sw,Sk} = 0.70$
$T_{mrt,r,KMM}$	K	T_{mrt} derived from radiant fluxes applying Equation (3)
$T_{mrt,Tg,BG}$	K	T_{mrt} of a black globe derived applying Equation (8) using measured T_g, T_a, v_a
v_a	m/s	air velocity
Greek		
α_{2K}, α_{5K}	%	error probability in the compliance with the accuracy in T_{mrt} according to the ISO 7726 comfort ($\pm 2 K$) or stress ($\pm 5 K$) class
$\alpha_{sw,Sk}$	-	short-wave absorption coefficient of skin/clothing
γ_s	degree	solar elevation
$\epsilon_{lw,Sk}$	-	long-wave emissivity of skin/clothing
ρ_s	-	short-wave surface albedo
σ_{SB}	$5.67 \cdot 10^{-8} W \cdot m^{-2} \cdot K^{-4}$	Stefan-Boltzmann constant

References

- Guideline VDI 3787/Part 2. Environmental Meteorology, Methods for the Human Biometeorological Evaluation of Climate and Air Quality for Urban and Regional Planning at Regional Level: Part I: Climate. Kommission Reinhaltung der Luft im VDI und DIN-Normenausschuss KRdL. In *VDI/DIN Handbuch Reinhaltung der Luft, Band 1B: Umweltmeteorologie*; Beuth: Berlin, Germany, 2008.
- Staiger, H.; Laschewski, G.; Matzarakis, A. Selection of Appropriate Thermal Indices for Applications in Human Biometeorological Studies. *Atmosphere* **2019**, *10*, 18. [[CrossRef](#)]
- Parsons, K.C. Environments. In *The Effects of Hot, Moderate, and Cold Environments on Human Health, Comfort and Performance*; Taylor & Francis: New York, NY, USA, 2003; p. 518. ISBN 0-415-23793-9.
- Kantor, N.; Unger, J. The most problematic variable in the course of human-biometeorological comfort assessment—The mean radiant temperature. *Cent. Eur. J. Geosci.* **2011**, *3*, 90–100. [[CrossRef](#)]
- Bohnenkamp, H.; Pasquay, W. Untersuchungen zu den Grundlagen des Energie- und Stoffwechsels. III. Mitteilung: Ein neuer Weg zur Bestimmung der für die Wärme-strahlung maßgebenden Oberfläche des Menschen. Die "mittlere Strahlungstemperatur". *Pflüger's Archiv* **1931**, *228*, 79–99. [[CrossRef](#)]
- Fanger, P.O. Thermal Comfort. In *Analysis and Applications in Environmental Engineering*; McGraw-Hill Company: Detroit, MI, USA, 1972; p. 244.
- Gagge, A.P.; Fobelets, A.P.; Berglund, P.E. A Standard Predictive Index of Human Response to the Thermal Environment. *ASHRAE Trans.* **1986**, *92*, 709–731.

8. ISO. ISO 7726. *Ergonomics of the Thermal Environment—Instruments for Measuring Physical Quantities*, 2nd ed.; International Standard ISO 7726:1998 from Technical Committee ISO/TC 159; ISO: Berlin, Germany, 1998.
9. ASHRAE. *ASHRAE Handbook: Fundamentals*, 8th ed.; American Society of Heating and Air-Conditioning Engineers: Atlanta, GA, USA, 2001; p. 29. ISBN 1-931862-70-2.
10. Kubaha, K.; Fiala, D.; Toftum, J.; Taki, A.H. Human projected area factors for detailed direct and diffuse solar radiation analysis. *Int. J. Biometeorol.* **2004**, *49*, 113–129. [[CrossRef](#)]
11. Park, S.; Tuller, S.E. Human body area factors for radiation exchange analysis: Standing and walking postures. *Int. J. Biometeorol.* **2011**, *55*, 695–709. [[CrossRef](#)]
12. Jendritzky, G.; Menz, G.; Schmidt-Kessen, W.; Schirmer, H. *Methode zur Raumbelastungs-Bewertung der Thermischen Komponente im Bioklima des Menschen (Fortgeschriebenes Klima-Michel-Modell)*; Akademie für Raumforschung und Landesplanung: Hannover, Germany, 1990; p. 80. ISBN 3888382076.
13. Ohmura, A.; Dutton, E.G.; Forgan, B.; Fröhlich, C.; Gilgen, H.; Hegner, H.; Heimo, A.; König-Langlo, G.; McArthur, B.; Müller, G.; et al. Baseline Surface Radiation Network (BSRN/WRCP): New Precision Radiometry for Climate Research. *Bull. Am. Meteor. Soc.* **1998**, *79*, 2115–2136. [[CrossRef](#)]
14. WMO. *Guide to Meteorological Instruments and Methods of Observation*, 2008th ed.; WMO No. 8; updated 2010; World Meteorological Organization: Geneva, Switzerland, 2010; ISBN 978-92-63-10008-5.
15. Höpfe, P. Ein neues Verfahren zur Bestimmung der mittleren Strahlungstemperatur im Freien. *Wetter und Leben* **1992**, *44*, 147–151.
16. Bedford, T.; Warner, C.G. The globe thermometer in studies of heating and ventilation. *Epidemiol. Infect.* **1934**, *34*, 458–473. [[CrossRef](#)]
17. Vernon, H.M. The measurement of radiant heat in relation to human comfort. *J. Ind. Hyg.* **1932**, *14*, 95–111.
18. Yaglou, C.P.; Minard, C.D. Control of heat casualties at military training centers. *AMA Arch. Ind. Health* **1957**, *16*, 302–316. [[PubMed](#)]
19. ISO. ISO 7243: *Hot Environments—Estimation of the Heat Stress on Working Man, Based on the WBGT-Index (Wet Bulb Globe Temperature)*, 2nd ed.; Reference number ISO 7243; ISO: Geneva, Switzerland, 1989.
20. Nikolopoulou, M.; Baker, N.; Steemers, K. Improvements to the Globe Thermometer for Outdoor Use. *Archit. Sci. Rev.* **1999**, *42*, 27–34. [[CrossRef](#)]
21. Thorsson, S.; Lindberg, F.; Eliasson, I.; Holmér, B. Different methods for estimating the mean radiant temperature in an outdoor urban setting. *Int. J. Climatol.* **2007**, *27*, 1983–1993. [[CrossRef](#)]
22. ASHRAE. *ASHRAE Handbook, Fundamentals*, 4th ed.; American Society of Heating, Refrigerating, and Air-Conditioning Engineers Inc.: Atlanta, GA, USA, 2001; p. 34.
23. Perez, R.; Ineichen, P.; Seals, R.; Zelenka, A. Making full use of the clearness index for parameterizing hourly insolation conditions. *Sol. Energy* **1990**, *45*, 111–114. [[CrossRef](#)]
24. Gaspar, A.R.; Quintela, D.A. Physical modelling of globe and natural wet bulb temperatures to predict WBGT heat stress index in outdoor environments. *Int. J. Biometeorol.* **2009**, *53*, 221–230. [[CrossRef](#)] [[PubMed](#)]
25. Gueymard, C.A. Direct and indirect uncertainties in the prediction of tilted irradiance for solar engineering applications. *Sol. Energy* **2009**, *83*, 432–444. [[CrossRef](#)]
26. Hodder, S.G.; Parsons, K.C. The effects of solar radiation on thermal comfort. *Int. J. Biometeorol.* **2007**, *51*, 233–250. [[CrossRef](#)]
27. Battles, F.J.; Olmo, F.J.; Alados-Arboledas, L. On shadowband correction methods for diffuse irradiance measurements. *Sol. Energy* **1995**, *54*, 105–114. [[CrossRef](#)]
28. Sanchez, G.; Serrano, A.; Cancillo, M.L.; Garcia, J.A. Comparison of shadow-ring correction models for diffuse solar irradiance. *J. Geophys. Res.* **2012**, *117*, 8. [[CrossRef](#)]
29. Ineichen, P.; Guisan, O.; Perez, R. Ground-reflected radiation and albedo. *Sol. Energy* **1990**, *44*, 207–214. [[CrossRef](#)]
30. Staiger, H. Die Strahlungskomponente im Thermischen Wirkungskomplex für Operationelle Anwendungen in der Human-Biometeorologie. Ph.D. Thesis, University of Freiburg, Freiburg, Germany, 2014; p. 287.
31. Reindl, D.T.; Beckman, W.A.; Duffie, J.A. Diffuse fraction correlations. *Sol. Energy* **1990**, *45*, 1–7. [[CrossRef](#)]
32. Muneer, T.; Gueymard, C.; Kambezidis, H. *Solar Radiation and Daylight Models*, 2nd ed.; Butterworth-Heinemann: Oxford, UK, 2004; p. 345. ISBN 0 7506 5974 2.
33. VDI 3786/Part 5: Environmental meteorology: Meteorological measurements: Radiation. Kommission Reinhaltung der Luft im VDI und DIN-Normenausschuss KRdL. In *VDI/DIN Handbuch Reinhaltung der Luft, Band 1B: Umweltmeteorologie*; Beuth: Berlin, Germany, 2015.

34. Liljegren, J.C.; Carhart, R.A.; Lawday, P.; Tschopp, S.; Sharp, R. Modeling the wet bulb globe temperature using standard meteorological measurements. *J. Occup. Environ. Hyg.* **2008**, *5*, 645–655. [[CrossRef](#)] [[PubMed](#)]
35. Graves, K.W. Globe thermometer evaluation. *Am. Ind. Hyg. Ass. J.* **1974**, *35*, 30–40. [[CrossRef](#)] [[PubMed](#)]
36. Hellon, R.F.; Crockford, G.W. Improvements to the globe thermometer. *J. Appl. Physiol.* **1959**, *14*, 649–650. [[CrossRef](#)]
37. Fontana, L. Experimental study on the globe thermometer behaviour in conditions of asymmetry of the radiant temperature. *Appl. Therm. Eng.* **2010**, *30*, 732–740. [[CrossRef](#)]
38. Berglund, L.G. Radiation Measurement for Thermal Comfort Assessment in the Built Environment. In Thermal—Analysis—Human Comfort—Indoor Environments. In Proceedings of the Symposium Held at the National Bureau of Standards, Gaithersburg, MA, USA, 11 February 1977; National Bureau of Standards: Gaithersburg, MA, USA, 1977; pp. 117–130.
39. Kuehn, L.A.; Stubbs, R.A.; Weaver, R.S. Theory of the globe thermometer. *J. Appl. Physiol.* **1970**, *29*, 750–757. [[CrossRef](#)]
40. Stolwijk, J.A.J.; Hardy, J.D.D. Temperature regulation in man—A theoretical study. *Pflügers Archiv* **1966**, *291*, 129–162. [[CrossRef](#)]
41. Gueymard, C.A.; Myers, D.R. Evaluation of conventional and high-performance routine solar radiation measurements for improved solar resource, climatological trends, and radiative modeling. *Sol. Energy* **2009**, *83*, 171–185. [[CrossRef](#)]
42. Dehne, K.; Bergholter, U.; Kasten, F. *IEA Comparison of Longwave Radiometers*; Report No. IEA-SHCP-9F-3; Deutscher Wetterdienst: Hamburg, Germany, 1993; p. 70.
43. *Technische Normen, Gütevorschriften, Lieferungsbedingungen DDR (TGL) 32603/2: Arbeitshygiene, Mikroklima in Arbeitsräumen, Meßmethode*; BBSR: Berlin, Germany, 1975.
44. Töpfer, M.; Garbatzok, M.; Bendisch, F. *Bioklimaprogramm—Datenerfassungsprogramm*; Forschungsinstitut für Bioklimatologie, Meteorologischer Dienst der DDR: Berlin, Germany, 1983.
45. Kantor, N.; Lin, T.-P.; Matzarakis, A. Daytime relapse of the mean radiant temperature based on the six-directional method under unobstructed solar radiation. *Int. J. Biometeorol.* **2014**, *58*, 1615–1625. [[CrossRef](#)]
46. Chen, Y.-C.; Lin, T.-P.; Matzarakis, A. Comparison of mean radiant temperature from field experiment and modelling: A case study in Freiburg, Germany. *Theor. Appl. Climatol.* **2014**, *118*, 535–551. [[CrossRef](#)]
47. Holmer, B.; Lindberg, F.; Rayner, D.; Thorsson, S. How to transform the standing man from a box to a cylinder—A modified methodology to calculate mean radiant temperature in field studies and models. In Proceedings of the 9th International Conference on Urban Climate (ICUC9), Toulouse, France, 20–24 July 2015; p. 6.
48. WMO. *Manual on Codes—International Codes—Volume I.1-Part A—Alphanumeric Codes*; WMO-No. 306; World Meteorological Organization: Geneva, Switzerland, 2009; ISBN 978-92-63-10306-2.
49. Buonanno, G.; Frattolillo, A.; Vanoli, L. Direct and indirect measurement of WBGT index in transversal flow. *Measurement* **2001**, *29*, 127–135. [[CrossRef](#)]
50. Bernard, T.E.; Barrow, C.A. Empirical approach to outdoor WBGT from meteorological data and performance of two different instrument designs. *Ind. Health* **2013**, *51*, 79–85. [[CrossRef](#)]
51. Sullivan, C.D.; Gorton, R.L. A method of calculation of WBGT from environmental factors. *ASHRAE Trans.* **1976**, *82*, 279–292.
52. Azer, N.Z.; Hsu, S. OSHA heat stress standards and the WBGT index. *ASHRAE Trans.* **1977**, *83*, 30–40.
53. Hunter, C.H.; Minyard, C.O. *Estimating Wet Bulb Globe Temperature Using Standard Meteorological Measurements*; WSRCMS-99-00757; Department of Energy (DOE), Office of Scientific and Technical Information (OSTI), Westinghouse Savannah River Company: Aiken, SC, USA, 1999.
54. Turco, S.H.N.; da Silva, T.G.F.; de Oliveira, G.M.; Leitao, M.M.V.B.R.; de Moura, M.S.B.; Pinheiro, C.; da Silva Padilha, C.V. Estimating black globe temperature based on meteorological data. In Proceedings of the Livestock Environment VIII, Iguassa Falls, Brazil, 31 August–4 September 2008; p. 6. [[CrossRef](#)]
55. Wang, S.; Li, Y. Suitability of acrylic and copper globe thermometers for diurnal outdoor settings. *Build. Environ.* **2015**, *98*, 279–294. [[CrossRef](#)]
56. Bond, T.E.; Kelly, C.F. The globe thermometer in agricultural research. *Agric. Eng.* **1955**, *36*, 251–255.
57. Büttner, K. *Physikalische Bioklimatologie—Probleme und Methoden*; Akademische Verlagsgesellschaft m.b.H.: Leipzig, Germany, 1938; p. 153.

58. Kee, R.J.; Landram, C.S.; Miles, J.C. Natural convection of a heat-generating fluid within closed vertical cylinders and spheres. *J. Heat Transfer*. **1976**, *98*, 55–61. [[CrossRef](#)]
59. Hey, E.N. Small globe thermometers. *J. Phys. E Sci. Instrum.* **1968**, *1*, 955–957. [[CrossRef](#)]
60. Hatch, T.F. Design requirements and limitations of a single-reading heat stress meter. *Am. Ind. Hyg. Assoc. J.* **1973**, *34*, 66–72. [[CrossRef](#)]
61. Fountain, M. *Instrumentation for thermal comfort measurements: The globe thermometer*; Internal study, Centre for the Built Environment, Series Indoor Quality (IEQ), University of California: Berkeley, CA, USA, 1987; Available online: <http://escholarship.org/uc/item/1qx8c7sm> (accessed on 24 July 2020).
62. Juang, Y.-J.; Lin, Y.-C. The Effect of Thermal Factors on the Measurement of Wet Bulb Globe Temperature. *J. Occup. Saf. Health* **2007**, *15*, 191–203. [[CrossRef](#)]
63. Vincent, D.F. Improvements in the globe thermometer. *J. Hyg. Camb.* **1939**, *39*, 238–243. [[CrossRef](#)] [[PubMed](#)]
64. Humphreys, M.A. The optimum diameter for a globe thermometer for use indoors. *Ann. Occup. Hyg.* **1977**, *20*, 135–140. [[CrossRef](#)] [[PubMed](#)]
65. De Dear, R. Ping-pong globe thermometers for mean radiant temperatures. *Heat. Vent. Eng.* **1988**, *60*, 10–11.
66. Epstein, Y.; Moran, D.S. Thermal comfort and the heat stress indices. *Ind. Health* **2006**, *44*, 388–398. [[CrossRef](#)]
67. Lemke, B.; Kjellstrom, T. Calculating workplace WBGT from meteorological data: A tool for climate change assessment. *Ind. Health* **2012**, *50*, 267–268. [[CrossRef](#)] [[PubMed](#)]
68. D’Ambrosio Alfano, F.R.; Malchaire, J.; Paella, B.I.; Riccio, G. WBGT Index revisited after 60 years of use. *Ann. Occup. Hyg.* **2014**, *58*, 955–970. [[CrossRef](#)] [[PubMed](#)]
69. Hardcastle, S.; Butler, K. A comparison of globe, wet and dry temperature and humidity measuring devices available for heat stress assessment. In Proceedings of the 12th US/North American Mine Ventilation Symposium, Reno, NV, USA, 9–11 June 2008; pp. 181–190, ISBN 978-0-615-20009-5.
70. Kantor, N.; Kovacs, A.; Lin, T.-P. Looking for simple correction functions between the mean radiant temperature from the “standard black globe” and the “six-directional” techniques in Taiwan. *Theor. Appl. Climatol.* **2015**, *121*, 99–111. [[CrossRef](#)]
71. Wilbert, S.; Kleindiek, S.; Nouri, B.; Geuder, N.; Habte, A.; Schwandt, M.; Vignola, F. Uncertainty of rotating shadowband irradiometers and Si-pyranometers including the spectral irradiance error. *AIP Conf. Proc.* **1734**, *1734*, 11. [[CrossRef](#)]
72. Vuilleumier, L.; Felix, C.; Vignola, F.; Blanc, P.; Badosa, J.; Kazantzidis, A.; Calpini, B. Performance Evaluation of Radiation Sensors for the Solar Energy Sector. *Meteorologische Zeitschrift* **2017**, *26*, 485–505. [[CrossRef](#)]
73. Lindberg, F.; Holmer, B.; Thorsson, S. SOLWEIG 1.0—Modelling spatial variations of 3D radiant fluxes and mean radiant temperature in complex urban settings. *Int. J. Biometeorol.* **2008**, *52*, 697–713. [[CrossRef](#)]
74. Huttner, S.; Bruse, M. Numerical modeling of the urban climate—A preview on ENVI-MET 4.0. In Proceedings of the Seventh International Conference on Urban Climate (ICUC7), Yokohama, Japan, 29 June—3 July 2009; p. 4.
75. Matzarakis, A.; Matuschek, O. Sky view factor as a parameter in applied climatology—Rapid estimation by the SkyHelios model. *Meteorologische Zeitschrift* **2011**, *20*, 39–45. [[CrossRef](#)]
76. Weihs, P.; Staiger, H.; Tinz, B.; Batchvarova, E.; Rieder, H.; Vuilleumier, L.; Maturille, M.; Jendritzky, G. The uncertainty of UTCI due to uncertainties in the determination of radiation fluxes derived from measured and observed meteorological data. *Int. J. Biometeorol.* **2012**, *56*, 537–555. [[CrossRef](#)] [[PubMed](#)]
77. Pappenberger, F.; Jendritzky, G.; Staiger, H.; Dutra, E.; Di Giuseppe, F.; Richardson, D.S.; Cloke, H.L. Global forecasting of thermal health hazards: The skill of probabilistic predictions of the Universal Thermal Climate Index (UTCI). *Int. J. Biometeorol.* **2015**, *59*, 311–323. [[CrossRef](#)] [[PubMed](#)]
78. Krähenmann, S.; Walter, A.; Brienen, S.; Imbery, F.; Matzarakis, A. High-resolution grids of hourly meteorological variables for Germany. *Theor. Appl. Climatol.* **2018**, *131*, 899–926. [[CrossRef](#)]
79. Rosenfelder, M.; Koppe, C.; Pfafferoth, J.; Matzarakis, A. Effects of ventilation behaviour on indoor heat load based on test reference years. *Int. J. Biometeorol.* **2016**, *60*, 277–287. [[CrossRef](#)]

